NANO LETTERS

Letter

pubs.acs.org/NanoLett

Spatially Resolved Imaging on Photocarrier Generations and Band Alignments at Perovskite/PbI_2 Heterointerfaces of Perovskite Solar Cells by Light-Modulated Scanning Tunneling Microscopy

Min-Chuan Shih,[†] Shao-Sian Li,[‡] Cheng-Hua Hsieh,[†] Ying-Chiao Wang,[‡] Hung-Duen Yang,[†] Ya-Ping Chiu,*[,†,§,∥,#] Chia-Seng Chang,[∥] and Chun-Wei Chen*[,‡,#]

[†]Department of Physics, National Sun Yat-sen University, Kaohsiung 804, Taiwan

[‡]Department of Materials Science and Engineering and [§]Department of Physics, National Taiwan University, Taipei 106, Taiwan

[∥]Institute of Physics, Academia Sinica, Nankang, Taipei 115, Taiwan

[#]Taiwan Consortium of Emergent Crystalline Materials (TCECM), Ministry of Science and Technology, Taipei 106, Taiwan

S *Supporting Information*

ABSTRACT: The presence of the PbI_2 passivation layers at perovskite crystal grains has been found to considerably affect the charge carrier transport behaviors and device performance of perovskite solar cells. This work demonstrates the application of a novel light-modulated scanning tunneling microscopy (LM-STM) technique to reveal the interfacial electronic structures at the heterointerfaces between $CH_3NH_3PbI_3$ perovskite crystals and PbI_2 passivation layers of individual perovskite grains under light illumination. Most importantly, this technique enabled the first observation of spatially resolved mapping images of photoinduced interfacial band bending of valence bands and conduction bands and the photogenerated electron and hole carriers at the heterointerfaces of perovskite crystal grains. By systematically exploring the interfacial electronic structures of individual perovskite grains, enhanced charge separation and reduced back recombination were observed when an optimal design of interfacial PbI_2 passivation layers consisting of a thickness less than 20 nm at perovskite crystal grains was applied.

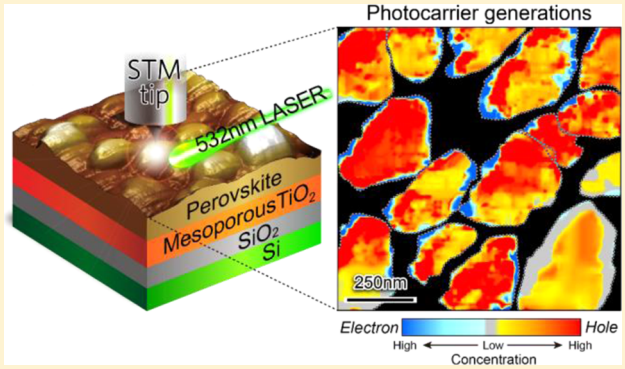

KEYWORDS: *Perovskite-based solar cells, PbI_2 passivation layer, heterointerface, scanning tunneling spectroscopy*

Organic−inorganic hybrid perovskite materials of $CH_3NH_3PbX_3$ (X = Cl, Br, I) have recently shown the power conversion efficiencies up to 20%[1,2] in photovoltaic applications. This is because they possess the excellent physical properties such as high optical absorption coefficients,[3−5] high carrier mobility, and long and balanced electron−hole diffusion lengths.[6] Numerous efforts have been conducted on fabricating high-quality perovskite films by controlling their morphologies,[7−9] coverage, grain sizes, or degree of crystallinity through thermal annealing, solvent engineering,[10] and incorporation of small amounts of chemical additives.[11−13] The inherent polycrystallinity of perovskite films is expected to significantly affect the charge generation and transport efficiency under light illumination.[14−19] Recently, Chen et al. reported that precipitating an optimal thin PbI_2 layer at the surrounding regions of perovskite crystal grains during post-thermal annealing may considerably improve the device performance, and this is because the presence of PbI_2 layers at perovskite crystal grains engenders successful passivation that affects carrier transport behaviors along heterojunctions.[20,21] However, although the presence of an optimal thin PbI_2 layer at perovskite crystals may enhance the device performance, a detailed understanding of local electronic information regarding carrier generation and transport at the heterointerfaces of the perovskite crystal grains and the passivation layers is still not achieved. Accordingly, a full investigation of local electronic structures of the heterointerfaces between the $CH_3NH_3PbI_3$ crystal grains and PbI_2 passivation layers of perovskite films will be of crucial importance to further enhance the performance and stability of perovskite-based photovoltaic devices. Previously, atomic force microscopy (AFM) and Kelvin probe force microscopy (KPFM) have been employed to explore the local electronic structures of perovskite photovoltaic materials. Both techniques typically provide information based on the contact potential difference (CPD), with which the corresponding work functions of composed materials can be inferred.[14,20−24] Nevertheless, because photogenerated electrons and holes must be transported through the valence bands (VBs) and conduction bands (CBs) of individual device

Received: November 17, 2016
Revised: January 9, 2017
Published: January 17, 2017

DOI: 10.1021/acs.nanolett.6b04803
Nano Lett. 2017, 17, 1154−1160

constituents, one should achieve a more comprehensive understanding of charge separation and transport behavior toward two opposite electrodes by directly revealing the interfacial band alignments of VBs and CBs at perovskite crystals. Scanning tunneling microscopy (STM) combined with scanning tunneling spectroscopy (STS) has the unique advantage of providing the local electronic density of states (LDOS) with spatial resolution at a nanometer scale or even atomic scale.[25] Therefore, STM may be an ideal tool for exploring local electronic information regarding interfacial band alignments and the corresponding charge generation behaviors at the heterointerfaces of perovskite crystal grains. In this work, we employed a light-modulated STM (LM-STM) technique[26,27] to reveal the correlation between nanoscale compositional distributions and interfacial electronic structures of heterointerfaces between the $CH_3NH_3PbI_3$ perovskite crystals and PbI_2 passivation layers under light illumination. Detailed descriptions of the LM-STM setup are provided in the Experimental Section and Supporting Information 1. Most importantly, this technique enabled the first observation of spatially resolved imaging on photoinduced interfacial band bending of VBs and CBs and photogenerated carriers at the heterointerfaces of perovskite crystal grains. The result allows us to understand the important role of the PbI_2 passivation layers at perovskite crystal grains on the behaviors of carrier generation and recombination for further improving the power conversion efficiencies of perovskite solar cells.

Results and Discussion. *Sample Characteristics.* Figure 1a shows a cross-sectional scanning electron microscope (SEM) image of a $CH_3NH_3PbI_3$ perovskite solar cell. The device architecture comprised FTO/TiO_2/$CH_3NH_3PbI_3$/spiro-OMeTAD fabricated using the conventional sequential deposition process (two-step process) which has been addressed in detail in the Supporting Information. The resulting mesoscopic $CH_3NH_3PbI_3$ perovskite-based solar cell exhibited promising device performance, as shown in Figure 1b, with an open-circuit voltage (V_{oc}) of 1.02 V, a current density (J_{sc}) of 21.2 mA/cm^2, a fill factor (FF) of 69.6%, and a PCE of 15.06%. Details about the device fabrication procedures and device performance are provided in the Experimental Section. Figure 1c presents a top-view SEM image of a perovskite thin film before the deposition of a hole transporting layer (HTL) of spiro-OMeTAD. This image reveals a granular morphology comprising many isolated $CH_3NH_3PbI_3$ grains with sizes of approximately 200−600 nm, similar to morphological observations in previous reports.[10,22,28] The isolated granular morphology is more commonly observed in the perovskite films using the two-step sequential deposition process, which allows us to systematically explore the interfacial electronic structures of *individual* perovskite crystal grains without being affected by each other in the following STM measurements. The compositions of the perovskite thin film after thermal annealing were measured by the X-ray diffraction (XRD) as shown in Supporting Information 2 (Figure S2). Strong diffraction peaks were observed at 14.2° and 28.5°, assigned to the (110) and (220) planes of the tetragonal $CH_3NH_3PbI_3$ perovskite lattice, whereas a lower diffraction peak at 12° corresponded to the (001) plane of the PbI_2 lattice, indicating the presence of PbI_2 in the $CH_3NH_3PbI_3$ perovskite thin film (Figure S2). To further understand how the presence of the PbI_2 passivation layer affects carrier generation and transport at perovskite crystals, we used an LM-STM in the ultrahigh vacuum (UHV) condition equipped with a light source (laser diode, λ = 532 nm, power intensity = 3 mW/cm^2) to perform real-space observations of photoinduced carrier generation and band alignments at heterointerfaces between the $CH_3NH_3PbI_3$ perovskite crystals and the PbI_2 passivation layers at nanometer spatial resolution, as schematically shown in Figure 1d. Because there is distinct difference at the absorption spectra of $CH_3NH_3PbI_3$ and PbI_2 (as shown in Figure S3), the light illumination at a wavelength of 532 nm was used for excitation to ensure that photocarrier generation of electrons and holes mainly occurred in the $CH_3NH_3PbI_3$ region rather than in the PbI_2 region. In addition, the electronic control system was used to replace the conventional mechanical chopper to effectively reduce the thermal effect in the LM-STM spectroscopic measurement. The detailed description of the electronic control system in the LM-STM setup for STS measurements was also addressed in the Supporting Information 1. To prepare the sample for the LM-STM measurement, the original FTO substrate was replaced with a 550 μm silicon substrate; this is because the commonly used FTO electrode for perovskite solar cells is typically deposited on a 2 mm glass substrate, which is too thick to be compatible with our STM sample holder. In addition, a 300 nm dense SiO_2 layer was thermally grown using wet oxygen on top of Si substrate to prevent the photocurrent resulting from Si substrate contributing to the tunneling current (as shown in Figure S4). The device configuration consists of a TiO_2 compact layer, mesoporous TiO_2 scaffold, and $CH_3NH_3PbI_3$ photoactive layer which were sequentially deposited based on the identical procedures as mentioned above.

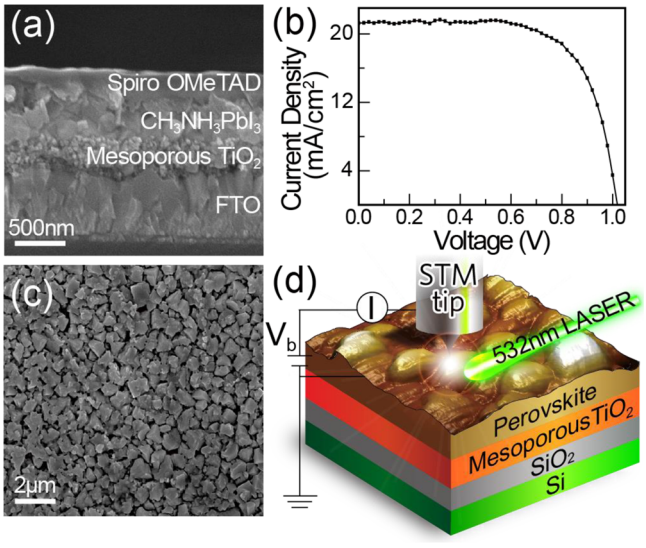

Figure 1. (a) SEM cross-sectional image of a $CH_3NH_3PbI_3$ perovskite solar cell with the architecture consisting of FTO/TiO_2/$CH_3NH_3PbI_3$/spiro-OMeTAD. (b) Current−voltage curves for the $CH_3NH_3PbI_3$ perovskite solar cell. (c) Top-view SEM image of the perovskite thin film before deposition of a hole transporting layer of spiro-OMeTAD. (d) Schematic description of the LM-STM measurement. The device configuration for LM-STM measurement is Si/SiO_2(300 nm)/TiO_2 compact layer/mesoporous TiO_2/perovskite crystals.

STM/STS Measurements in the Dark. Figure 2a exhibits a topographic STM image of the perovskite film measured in the dark, where the shapes of the perovskite crystal grains are outlined by the dashed curves. In the perovskite film, a number of grains with sizes of approximately 200−600 nm were clearly

DOI: 10.1021/acs.nanolett.6b04803
Nano Lett. 2017, 17, 1154−1160

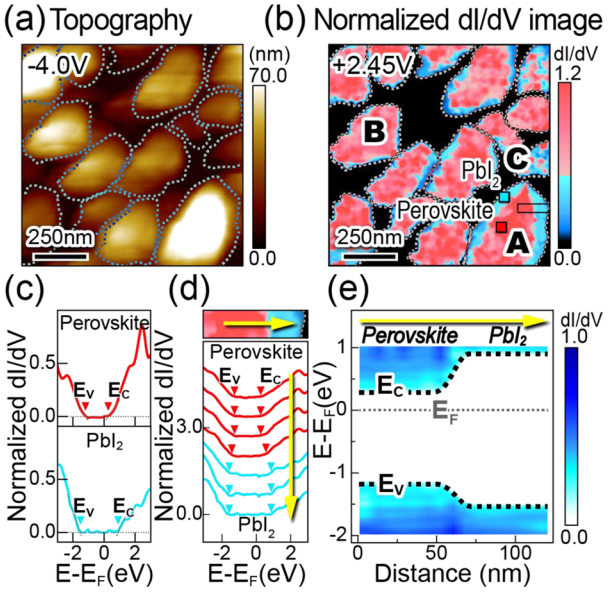

Figure 2. (a) Typical STM morphology image. (b) A mapping image of the normalized dI/dV spectra of the perovskite grains recorded at a sample bias of +2.45 V. (c) Two representative normalized dI/dV curves (lower and upper panels) obtained at the outer part of the grain (blue square in Grain A) and in the grain interior (red square in Grain A) respectively. (d) Point-to-point electronic dI/dV curves acquired across the perovskite/PbI_2 heterojunction in Grain A (denoted by the rectangular box in (b)). (e) A mapping image of the band alignment across the perovskite/PbI_2 heterointerface in Grain A by extracting the locations of the VB and CB edges indicated by the triangular marks in (d).

observed, which is consistent with the SEM observation presented in Figure 1c. To obtain the information on the compositional distribution within each grain, the normalized differential conductances (dI/dV) by means of the scanning tunneling spectroscopy (STS) measurements at the temperature of 100 K were used to reveal the density-of-states (DOS) information on individual constituents at perovskite grains, where the normalization procedure can eliminate the dI/dV dependency of the tip−sample separation in the STS measurement as the tip scans across the heterojunction.[29] Figure 2b shows the mapping image of the normalized dI/dV spectra of the perovskite grains recorded at the sample bias of +2.45 V. The electronic image of Figure 2b shows two distinct local electronic behaviors at the perovskite crystal grains. Larger dI/dV signals mostly appeared in grain interiors (colored by red), whereas lower dI/dV signals typically appeared at the outer parts of grains (colored by blue). The undetectable electronic signal level in the STS measurement due to the height difference among grains is viewed as the signal from the background, which is displayed by black in Figure 2b. We have also taken the effect of surface roughness of the perovskite crystals on the measurement into account. The discussion of the surface roughness effect on the STM measurement was also addressed in the Supporting Information 3. Figure 2c illustrates two representative normalized dI/dV curves as a function of the sample bias observed at the grain interior and at the outer part of Grain A, marked with red and blue squares, respectively. The position of the zero sample bias in the STM measurement is the Fermi level (E_F) of the system. The current onsets in the occupied and unoccupied states, corresponding to the VB and CB edges, respectively, were extracted (as indicated by the triangular marks) according to the methodology developed in ref 30. The representative dI/dV curve at the grain interior exhibited a more conductive feature compared with that observed at the outer part of the grain. The corresponding energy positions of the VB and CB edges (E_V/E_C) were at approximately −1.2 and +0.3 V respectively, indicating an estimated bandgap size of 1.5 eV (Figure 2c, upper panel). This type of curves were predominantly distributed in the interior regions of the perovskite grains, primarily resulting from the contribution of perovskite $CH_3NH_3PbI_3$ according to the reported value of the bandgap size.[31,32] By contrast, the representative dI/dV curve observed at the outer part of Grain A demonstrated less conductive features, and the specific onset biases of the VB and CB edges (E_V/E_C) were located at −1.5 and +0.9 V, respectively, exhibiting a bandgap size of approximately 2.4 eV (Figure 2c, lower panel). This type of curve can be attributed to the presence of PbI_2 thin layers, according to the similar band gap value obtained from the absorption spectrum and UPS data of PbI_2.[33] Due to the distinct electronic properties between perovskite $CH_3NH_3PbI_3$ and PbI_2, the distribution of the respective constituents at the perovskite crystal grains can be clearly distinguished from the corresponding normalized dI/dV curves. As shown in Figure 2b, Grain A consisted of a thicker (30−50 nm) PbI_2 layer, and Grain B consisted of a thinner (5−8 nm) PbI_2 layer at the corresponding perovskite crystal grains. In addition, some grains consisting of mixed $CH_3NH_3PbI_3$ and PbI_2 phases were also found on the top surface of the perovskite crystals (e.g., Grain C). Accordingly, the distinct electronic signals of the $CH_3NH_3PbI_3$ and PbI_2 dI/dV curves derived through STM/STS enabled obtaining the compositional distributions on the surface of individual perovskite grains at a nanometer-scaled resolution. The mapping image of the normalized dI/dV spectra obtained from STS measurement as shown in Figure 2b is consistent with the previous conclusion that thin PbI_2 passivation layers may be predominantly precipitated around the perovskite crystal grains after thermal annealing treatment.[20]

To further explore the band alignment at the heterointerfaces between the perovskite crystals and the PbI_2 passivation layers of individual perosvkite grains, Figure 2d exhibited the evolution of some representative tunneling spectra as a function of the sample bias acquired across the perovskite/PbI_2 heterojunction at Grain A (denoted by the rectangular box in Figure 2b). Extracting the locations of the VB and CB edges indicated by the triangular mark yielded a mapping image of the band alignment across the perovskite/PbI_2 heterointerface in Grain A as shown in Figure 2e, according to the electronic characteristics of the spatially dependent spectroscopic curves in Figure 2d. The energy band offsets of the VB and CB edges for $CH_3NH_3PbI_3$ and PbI_2 were approximately 0.3 and 0.6 eV, respectively, revealing a typical type I heterojunction at the perovskite/PbI_2 interface. In addition, both $CH_3NH_3PbI_3$ in the grain interior and PbI_2 at the outer part of the grain exhibited intrinsic n-type electronic behaviors with their Fermi levels being close to the corresponding CB edges, which is also consistent with previously reported UPS results.[34,35] Compared with the conventional techniques that generally measure the ionization potentials or electron affinities of individual components to obtain energy diagrams of a heterojunction structure,[34,36,37] the unique advantage of the STM/STS measurement enable directly visualizing spatially resolved band alignment characteristics and electronic configurations

DOI: 10.1021/acs.nanolett.6b04803
Nano Lett. 2017, 17, 1154−1160

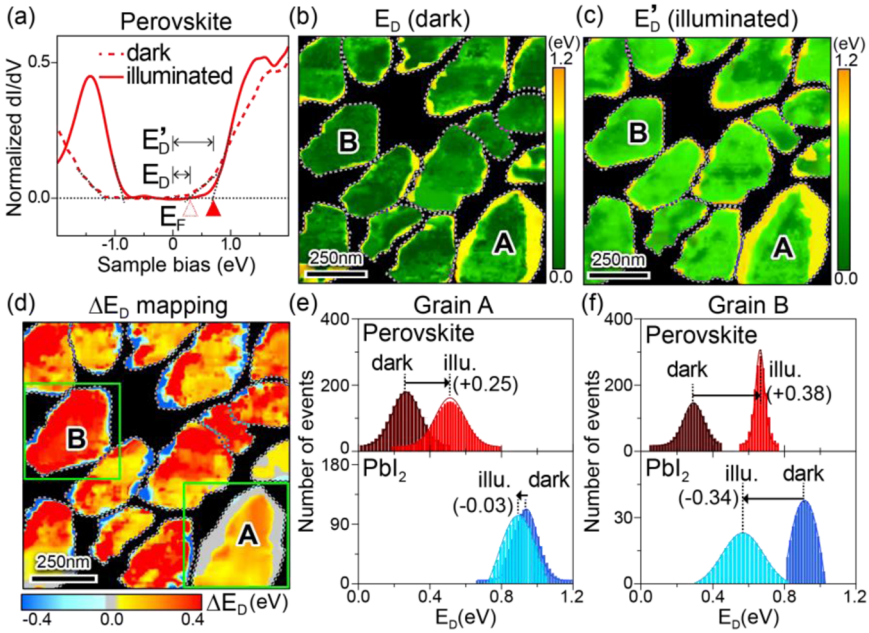

Figure 3. (a) Representative dI/dV curves of perovskites in dark (dashed curve) and under light illumination (solid curve) conditions. Imaging of the spatial distribution of the E_D and E_D' values derived for the perovskite grains (b) in the dark and (c) under illumination. (d) A mapping image of the spatial distributions of ΔE_D values ($\Delta E_D = E_D' - E_D$) observed for the perovskite grains under light illumination. The statistical histograms of all of the E_D values in (e) Grain A and (f) Grain B measured in the dark and under illumination, respectively.

across the $CH_3NH_3PbI_3/PbI_2$ heterojunctions of perovskite crystals.

Photocarrier Generations of Perovskites in STS Measurements under Illumination. Next, we applied the LM-STM technique to conduct real-space observations of the photoinduced charge transfer and band bending at the perovskite crystals under illumination. In typical semiconductors, the energy differences between the energetic positions of CB (VB) edges and Fermi levels can be used to estimate the carrier concentrations or carrier types of materials. Hence, the shift of the energy difference E_D between the energetic positions of the CB edge (E_C) and the Fermi level (E_F), denoted as $E_D = E_C - E_F$, can be used to characterize photoinduced charge transfer behaviors in perovskite grains under light illumination. The terms E_D and E_D', as shown in Figure 3a, represent the separation between the CB edges (E_C or E_C') and the Fermi level (E_F) in the dark and under illumination, respectively. The position of the CB edge (E_C) of the $CH_3NH_3PbI_3$ part (represented by the open red triangular symbol) was shifted toward a higher energy (E_C', indicated by the solid red triangular symbol) when the device was under light illumination, thus increasing the values of E_D to E_D'. In addition, an enhancement of the LDOS obtained from the dI/dV curve at a negative sample bias after light illumination was observed. This enhancement was mainly resulted from the increased tunneling current from the VB to the tip, indicating an increased carrier density of photoinduced holes in the $CH_3NH_3PbI_3$ parts of the perovskite grains (see the Supporting Information 4). Figure 3b and c present the distributions of the E_D and E_D' values derived for the perovskite grains in the dark and under illumination, respectively, where these E_D or E_D' values were obtained from the individual normalized dI/dV spectra at the perovskite crystals before and after light illumination. The stability of the LM-STS measurements is also discussed in the Supporting Information 5 and 6. When the device was under illumination, photoexcited carriers were generated and separated in the perovskite crystals, resulting in the variation of E_D and E_D'. Hence, the shifts of ΔE_D values, defined as $\Delta E_D = E_D' - E_D$, may be directly correlated with the variation of photogenerated carrier concentrations or carrier types as the device is under light illumination. Positive ΔE_D values are directly correlated with increases in hole concentrations as the energy difference between the CB edge and the Fermi level increases, whereas negative ΔE_D values are correlated with increases in electron concentrations as the CB edge is closer to the Fermi level after light illumination. Figure 3d exhibits a mapping image of the spatial distributions of ΔE_D values observed for the perovskite grains under light illumination. The ΔE_D values in the grain interiors were mostly positive (colored red or orange), whereas those at the outer parts of these grains were either negative (colored blue) or nearly zero (colored gray). Notably, the mapping image of these ΔE_D values at these perovskite grains shows a correlation to the compositional distributions of $CH_3NH_3PbI_3$ and PbI_2 as shown in Figure 2b, indicating that the shift of the ΔE_D values and the corresponding charge transfer behaviors strongly depend on the chemical compositions of perovskite grains. It is known that the $CH_3NH_3PbI_3$ perovskite material behaves as an ambipolar semiconductor with long electron−hole diffusion lengths,[38] although the intrinsic $CH_3NH_3PbI_3$ exhibits a Fermi level that is close to the CB edge.[34] A recent experimental result also revealed that photogenerated holes were extracted more efficiently than electrons in a $CH_3NH_3PbI_3$-based perovskite solar cell.[22] The positive ΔE_D values observed in the grain interiors ($CH_3NH_3PbI_3$ parts) are mainly attributed to the increased hole concentrations in these regions when the device was under light illumination, and these carriers can be collected effectively by inserting a HTL of spiro-OMeTAD, contributing to hole current.[37] Moreover, carefully examining the distributions in Figure 3d reveals that the quantities of positive ΔE_D values, and the corresponding increased hole concentrations strongly depend on the thickness of the PbI_2 passivation layers

DOI: 10.1021/acs.nanolett.6b04803
Nano Lett. 2017, 17, 1154−1160

at these grains. For the grains comprising a thin PbI_2 layer such as Grain B, the larger positive ΔE_D values indicated a considerable enhancement of hole concentrations in the grain interiors as the device was under light illumination. In addition, negative ΔE_D values were observed at the surrounding part of Grain B, and this is mainly attributed to an increased electron concentration, indicating that efficient charge separation also occurred at the heterointerface of Grain B. By contrast, the ΔE_D values at the outer part of Grain A, which consists of a thicker PbI_2 layer, remained nearly unchanged, indicating that charge separation at the heterointerface of Grain A is inefficient. The positive ΔE_D values observed in the interior regions ($CH_3NH_3PbI_3$ part) of Grain A were also found to be lower than those observed in the interior regions of Grain B. Figure 3e and f present the histograms of all of the E_D values in Grains A and B measured in the dark and under illumination, respectively. The average ΔE_D value in the interior region ($CH_3NH_3PbI_3$ part) of Grain A was approximately +0.25 eV, whereas that in the interior region of Grain B was approximately +0.40 eV. Moreover, the average ΔE_D value at the outer region (PbI_2 part) of the Grain A was nearly −0.03 eV, whereas that at the surrounding region of Grain B was approximately −0.34 eV, indicating efficient charge separation at the heterointerface of Grain B. These results suggest that the photoinduced charge generation behaviors at the $CH_3NH_3PbI_3/PbI_2$ heterointerface may strongly depend on the PbI_2 passivation layers at the perovskite crystal grains.

Band Alignments of Perovskites in STS Measurements under Illumination. To further reveal the effects of the thin PbI_2 layers on the photocarrier generation and separation at the heterointerface of the perovskite crystal grains, the interfacial band alignments across the perovskite/PbI_2 heterojunctions of Grains A and B as indicated by the colored solid arrows of Figure 4a and b were examined. Figures 4c–f illustrate the interfacial band alignments at Grains A and B in the dark and under light illumination derived from the characteristic curves of the point-to-point STS spectroscopic data. When the device was under illumination, a remarkable downward band bending was clearly observed in the PbI_2 region of Grain B (Figure 4d and f), whereas the energy shifts in the PbI_2 region of Grain A (Figure 4c and e) remained nearly intact. This result indicates that photogenerated electrons were efficiently transferred from the interior region of the $CH_3NH_3PbI_3$ part to the outer part of the PbI_2 region in Grain B, which comprised a thinner PbI_2 layer. By contrast, the thicker PbI_2 layer in Grain A not only hindered photoinduced charge transfer across the perovskite/PbI_2 interface but also increased the probability of carrier recombination. Accordingly, the increase in the hole concentration in the interior region of Grain A was considerably lower than that in Grain B as the device was under illumination, where the VB and CB edges shifted by only approximately 0.25 eV toward high energy levels (ΔE_D = +0.25 eV) in the perovskite region of Grain A compared to an approximately 0.40 eV shift in the perovskite region of Grain B (ΔE_D = +0.40 eV). Although the origin of the variation on the thickness of the PbI_2 passivation layers at the outer regions of perovskite crystal grains is not fully understood yet, one possible reason may be due to the nonuniform decomposition of $CH_3NH_3PbI_3$ during thermal annealing, which occurred at a moderate temperature by releasing CH_3NH_3I and precipitating PbI_2 phase.[20,39] It mostly occurred at the surrounding regions of perovskite grains because there are more defective sites than those at the grain interior areas.[40] By using the unique LM-STM measurements,

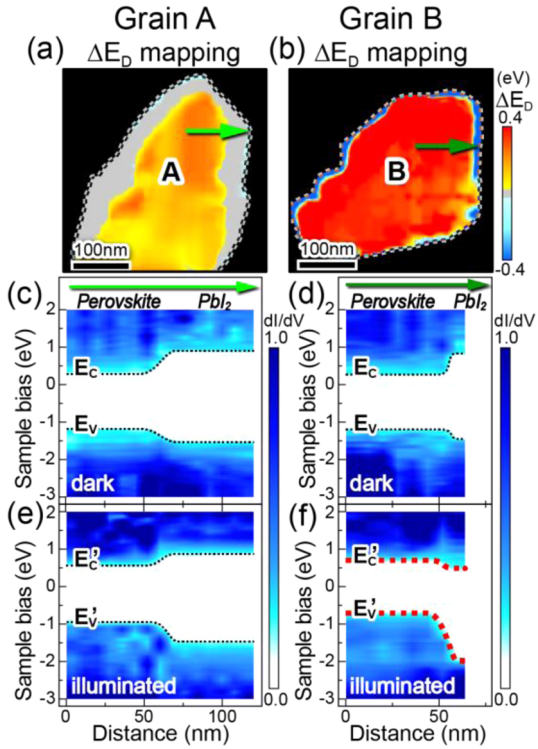

Figure 4. Perovskite grains of (a) Grain A and (b) Grain B selected from Figure 3d. (c) and (e) correspond to the band alignments across the heterojunctions (green arrows) of Grain A consisted of a thicker (~45 nm) PbI_2 layer in the dark and under light illumination, respectively. (d) and (f) correspond to the band alignments across the heterojunctions (green arrows) of Grain B consisted of a thinner (~8 nm) PbI_2 layer in the dark and under light illumination, respectively.

we are able to obtain the spatially resolved chemical compositions and interfacial band alignments simultaneously to correlate the photocarrier generation behaviors at the heterointerfaces of perovskite crystals.

PbI_2 Layer Thickness Dependence of ΔE_D. Figure 5 presents the dependence of the thickness of the PbI_2 passivation layers

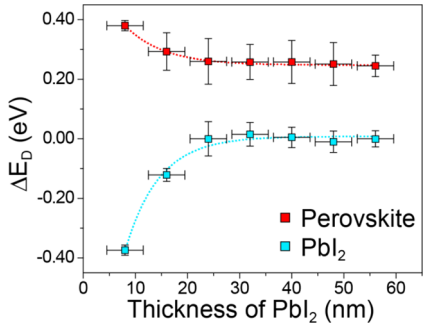

Figure 5. Dependence of the thickness of the PbI_2 passivation layers on the ΔE_D energy shifts obtained from statistical analyses of 12 perovskite crystal grains in the dark and with light illumination.

on the ΔE_D energy shifts obtained from statistical analyses of 12 perovskite crystal grains in our measurement. It was found that prominent photoinduced charge separation and transfer efficiencies at the heterointerfaces between the $CH_3NH_3PbI_3$ perovskite crystals and the PbI_2 passivation layers can be observed as the thickness of the PbI_2 layer is less than 20 nm, where the positive ΔE_D values corresponding to increased hole

DOI: 10.1021/acs.nanolett.6b04803
Nano Lett. 2017, 17, 1154–1160

concentrations at the $CH_3NH_3PbI_3$ parts (grain interiors) and the negative ΔE_D values corresponding to increased electron concentrations at the PbI_2 region (outer parts of grains) can be observed simultaneously. By contrast, when the thickness of the PbI_2 passivation layer was greater than 20 nm, the ΔE_D values in the PbI_2 regions were almost negligible, and the ΔE_D values at the $CH_3NH_3PbI_3$ parts (grain interiors) were nearly unchanged, indicating the occurrence of less efficient charge separation at the $CH_3NH_3PbI_3/PbI_2$ heterointerfaces of perovskite grains. Therefore, an optimal design of PbI_2 passivation layers at perovskite crystals can facilitate charge separation and prevent back recombination, consequently improving the device performance of perovskite solar cells. In such a design, efficient charge separation and transport of photogenerated carriers at the heterointerfaces of perovskite crystal grains may occur, where electrons can be transported through thin PbI_2 passivation layers to the electron transporting layer of TiO_2, and holes in $CH_3NH_3PbI_3$ parts can be collected effectively by the insertion of a hole transporting layer of spiro-OMeTAD, yielding lowest recombination loss.

Conclusion. We demonstrate the spatially resolved interfacial band alignments and photocarrier generation at heterointerfaces between the $CH_3NH_3PbI_3$ perovskite crystals and the PbI_2 passivation layers of individual perovskite grains using light-modulated scanning tunneling microscopy (LM-STM) technique. The result reveals the important role of the optimum PbI_2 passivation layers on the charge separation and recombination at perovskite crystal grains. The unique LM-STM technique enables conducting real-space observations of photocarrier generation and interfacial electronic structures at excellent spatial resolutions, and it has great potential for application in the future exploring other emerging energy systems of photovoltaic and photochemical cells.

Experimental Section. *Sample Characterizations and Device Fabrications.* FEI Nova NanoSEM 450 was used for the top-view SEM morphology observation of the perovskite thin films. For the XRD characterizations, Rigaku TTRAX 3 was used with Cu Kα (0.15418 nm) as an excitation source. For the perovskite solar cell fabrications, the TiO_2 compact layer was first deposited on the preclean FTO substrate using spin coating with 0.15 M titanium diisopropoxide bis-(acetylacetonate) (75% Aldrich) dissolved in 1-butanol (Aldrich) solution and was then thermally annealed at 70 °C for 5 min. Same chemicals with a concentration of 0.3 M was then spin coated and repeated twice on the previous TiO_2 layer and thermally annealed at 600 °C for 30 min to obtain the compact TiO_2 electron selective layer. Mesoporous TiO_2 was deposited by spin coating a commercial TiO_2 paste (Dyesol 18NRT, Dyesol) diluted in ethanol (2:7, weight ratio). After drying at 125 °C, the TiO_2 films were gradually heated to 600 °C in a furnace for 30 min.

The perovskite $CH_3NH_3PbI_3$ thin films were deposited using the sequential deposition process following ref 41. PbI_2 was dissolved in *N*,*N*-dimethylformamide at a concentration of 462 mg/mL (1 M), and CH_3NH_3I was dissolved in 2-propanol at a concentration of 10 mg/mL (0.0625 M). The PbI_2 solution was kept at 90 °C and spin-coated on mesoporous TiO_2 and dried at 90 °C for 30 min. After cooling to room temperature, the film was dipped in a solution of CH_3NH_3I for 20 s, rinsed with 2-propanol to remove the CH_3NH_3I residual, and then annealed at 90 °C for 30 min for the conversion of $CH_3NH_3PbI_3$ structure. The hole transporting layer, containing 0.170 M spiro-OMeTAD, 0.064 M bis(trifluoromethane)-sulfonimide lithium salt (Li-TFSI, 99.95%, Aldrich), and 0.198 M 4-*tert*-butylpyridine (TBP, 96%, Aldrich) in the mixed solvent of chlorobenzene (99.8%, Aldrich) and acetonitrile (99.8%, Aldrich) (chlorobenzene:acetonitrile = 1:0.1 v/v), was spin coated onto the $CH_3NH_3PbI_3$ layer followed by drying at 70 °C for 1 min. The top electrode of Au was then thermally evaporated in vacuum of 10^{-6} Torr. The photocurrent−voltage (J−V) characteristics (Keithley 2410 source meter) were obtained by using a solar simulator (Newport Inc.) with the A.M. 1.5 G filter under an irradiation intensity of 100 mW/cm^2.

LM-STM Experimental Setup and Sample Preparations. To prepare the perovskite sample for the LM-STM measurement, the FTO substrate was replace by a Si substrate with a dense 300 nm SiO_2 layer. The substrate was clean and treated with oxygen plasma. The following deposition of each layer was carried out using the procedures identical to those for the solar cell fabrication as mentioned above. Scanning tunneling spectroscopy (STS) measurements were performed at ∼100 K to obtain the local electronic structures across the perovskite grains.

The sample was illuminated with wavelength of 532 nm (correspond to an energy of 2.33 eV, which is large than the band gap of perovskite films) by a (3 ± 0.065) mW diode laser. The focusing of the beam spot was achieved by built-in lens at the coaxial rail with diode laser. The angle of the incidence laser was 50°. With the fine-tune system on the coaxial rail, the laser direction could be adjusted precisely to focus at the sample right below the tip position. The laser spot we focused below the tip position was elliptical (due to the inclined incident angle) with major and minor axes of (200 ± 20) μm and (100 ± 10) μm compared with the sample, which was determined with a long-focus microscope.

To reduce the thermal effect in our STS measurements with light illumination, we used the electronic control system to replace the conventional mechanical chopper. During the acquisition of current−voltage (I−V) spectra, the laser was electrically modulated by the STS control signal. Detailed parameters for the electrical modulations in STS measurements with light illumination are addressed in the Supporting Information 1.

■ ASSOCIATED CONTENT

Supporting Information

The Supporting Information is available free of charge on the ACS Publications website at DOI: 10.1021/acs.nanolett.6b04803.

Statements of the electrical modulations of light-modulated STM, material characterizations, surface roughness effect of perovskite films in STM measurements, electronic properties of perovskites under light illumination, stability of LM-STM measurement, and surface photovoltage (SPV) information on the perovskite solar cells (PDF)

■ AUTHOR INFORMATION

Corresponding Authors

*E-mail: ypchiu@phys.ntu.edu.tw.
*E-mail: chunwei@ntu.edu.tw.

ORCID

Ya-Ping Chiu: 0000-0001-7065-4411
Chun-Wei Chen: 0000-0003-3096-249X

DOI: 10.1021/acs.nanolett.6b04803
Nano Lett. 2017, 17, 1154−1160

Notes

The authors declare no competing financial interest.

■ ACKNOWLEDGMENTS

This work is supported by Minster of Science and Technology (MOST), Taiwan (Project No. 104-2112-M-003-015-MY3, 103-2112-M-003-013-MY3, and 103-2119-M-002-021-MY3, 104-2112-M-002-025-MY3, 103-2112-M-002-028-MY3) and Taiwan Consortium of Emergent Crystalline Materials (TCECM).

■ REFERENCES

(1) Green, M. A.; Emery, K.; Hishikawa, Y.; Warta, W.; Dunlop, E. D. *Prog. Photovoltaics* **2015**, *23*, 1−9.
(2) Jung, H. S.; Park, N.-G. *Small* **2015**, *11*, 10−25.
(3) Wehrenfennig, C.; Liu, M.; Snaith, H. J.; Johnston, M. B.; Herz, L. M. *J. Phys. Chem. Lett.* **2014**, *5*, 1300−1306.
(4) Sun, S. Y.; Salim, T.; Mathews, N.; Duchamp, M.; Boothroyd, C.; Xing, G. C.; Sum, T. C.; Lam, Y. M. *Energy Environ. Sci.* **2014**, *7*, 399−407.
(5) Green, M. A.; Ho-Baillie, A.; Snaith, H. J. *Nat. Photonics* **2014**, *8*, 506−514.
(6) Stranks, S. D.; Eperon, G. E.; Grancini, G.; Menelaou, C.; Alcocer, M. J. P.; Leijtens, T.; Herz, L. M.; Petrozza, A.; Snaith, H. J. *Science* **2013**, *342*, 341−344.
(7) Chen, Q.; Zhou, H.; Hong, Z.; Luo, S.; Duan, H.-S.; Wang, H.-H.; Liu, Y.; Li, G.; Yang, Y. *J. Am. Chem. Soc.* **2014**, *136*, 622−625.
(8) Nie, W.; Tsai, H.; Asadpour, R.; Blancon, J.-C.; Neukirch, A. J.; Gupta, G.; Crochet, J. J.; Chhowalla, M.; Tretiak, S.; Alam, M. A.; Wang, H.-L.; Mohite, A. D. *Science* **2015**, *347*, 522−525.
(9) Saliba, M.; Tan, K. W.; Sai, H.; Moore, D. T.; Scott, T.; Zhang, W.; Estroff, L. A.; Wiesner, U.; Snaith, H. J. *J. Phys. Chem. C* **2014**, *118*, 17171−17177.
(10) Dar, M. I.; Arora, N.; Gao, P.; Ahmad, S.; Grätzel, M.; Nazeeruddin, M. K. *Nano Lett.* **2014**, *14*, 6991−6996.
(11) Docampo, P.; Ball, J. M.; Darwich, M.; Eperon, G. E.; Snaith, H. J. *Nat. Commun.* **2013**, *4*, 2761.
(12) Liang, P.-W.; Liao, C.-Y.; Chueh, C.-C.; Zuo, F.; Williams, S. T.; Xin, X.-K.; Lin, J.; Jen, A. K. Y. *Adv. Mater.* **2014**, *26*, 3748−3754.
(13) Chang, C.-Y.; Chu, C.-Y.; Huang, Y.-C.; Huang, C.-W.; Chang, S.-Y.; Chen, C.-A.; Chao, C.-Y.; Su, W.-F. *ACS Appl. Mater. Interfaces* **2015**, *7*, 4955−4961.
(14) Yun, J. S.; Ho-Baillie, A.; Huang, S.; Woo, S. H.; Heo, Y.; Seidel, J.; Huang, F.; Cheng, Y. B.; Green, M. A. *J. Phys. Chem. Lett.* **2015**, *6*, 875−880.
(15) Yan, Y.; Jiang, C. S.; Noufi, R.; Wei, S. H.; Moutinho, H. R.; Al-Jassim, M. M. *Phys. Rev. Lett.* **2007**, *99*, 235504.
(16) Kawamura, M.; Yamada, T.; Suyama, N.; Yamada, A.; Konagai, M. *Jpn. J. Appl. Phys.* **2010**, *49*, 062301.
(17) Lim, K.-G.; Kim, H.-B.; Jeong, J.; Kim, H.; Kim, J. Y.; Lee, T.-W. *Adv. Mater.* **2014**, *26*, 6461−6466.
(18) Kim, H.; Lim, K.-G.; Lee, T.-W. *Energy Environ. Sci.* **2016**, *9*, 12−30.
(19) Lim, K.-G.; Ahn, S.; Kim, Y.-H.; Qi, Y.; Lee, T.-W. *Energy Environ. Sci.* **2016**, *9*, 932−939.
(20) Chen, Q.; Zhou, H.; Song, T. B.; Luo, S.; Hong, Z.; Duan, H. S.; Dou, L.; Liu, Y.; Yang, Y. *Nano Lett.* **2014**, *14*, 4158−4163.
(21) Edri, E.; Kirmayer, S.; Cahen, D.; Hodes, G. *J. Phys. Chem. Lett.* **2013**, *4*, 897−902.
(22) Edri, E.; Kirmayer, S.; Henning, A.; Mukhopadhyay, S.; Gartsman, K.; Rosenwaks, Y.; Hodes, G.; Cahen, D. *Nano Lett.* **2014**, *14*, 1000−1004.
(23) Bergmann, V. W.; Weber, S. A.; Javier Ramos, F.; Nazeeruddin, M. K.; Gratzel, M.; Li, D.; Domanski, A. L.; Lieberwirth, I.; Ahmad, S.; Berger, R. *Nat. Commun.* **2014**, *5*, 5001.
(24) Spadafora, E. J.; Demadrille, R.; Ratier, B.; Grevin, B. *Nano Lett.* **2010**, *10*, 3337−3342.
(25) Ohmann, R.; Ono, L. K.; Kim, H.-S.; Lin, H.; Lee, M. V.; Li, Y.; Park, N.-G.; Qi, Y. *J. Am. Chem. Soc.* **2015**, *137*, 16049−16054.
(26) Yoshida, S.; Kanitani, Y.; Oshima, R.; Okada, Y.; Takeuchi, O.; Shigekawa, H. *Phys. Rev. Lett.* **2007**, *98*, 026802.
(27) Takeuchi, O.; Yoshida, S.; Shigekawa, H. *Appl. Phys. Lett.* **2004**, *84*, 3645−3647.
(28) Laban, W. A.; Etgar, L. *Energy Environ. Sci.* **2013**, *6*, 3249−3253.
(29) Smith, A. R.; Gwo, S.; Sadra, K.; Shih, Y. C.; Streetman, B. G.; Shih, C. K. *J. Vac. Sci. Technol., B: Microelectron. Process. Phenom.* **1994**, *12*, 2610−2615.
(30) Feenstra, R. M. *Phys. Rev. B: Condens. Matter Mater. Phys.* **1994**, *50*, 4561−4570.
(31) Wu, K.; Bera, A.; Ma, C.; Du, Y.; Yang, Y.; Li, L.; Wu, T. *Phys. Chem. Chem. Phys.* **2014**, *16*, 22476−22481.
(32) Milot, R. L.; Eperon, G. E.; Snaith, H. J.; Johnston, M. B.; Herz, L. M. *Adv. Funct. Mater.* **2015**, *25*, 6218−6227.
(33) Cao, D. H.; Stoumpos, C. C.; Malliakas, C. D.; Katz, M. J.; Farha, O. K.; Hupp, J. T.; Kanatzidis, M. G. *APL Mater.* **2014**, *2*, 091101.
(34) Schulz, P.; Edri, E.; Kirmayer, S.; Hodes, G.; Cahen, D.; Kahn, A. *Energy Environ. Sci.* **2014**, *7*, 1377−1381.
(35) Ahuja, R.; Arwin, H.; Ferreira da Silva, A.; Persson, C.; Osorio-Guillén, J. M.; Souza de Almeida, J.; Moyses Araujo, C.; Veje, E.; Veissid, N.; An, C. Y.; Pepe, I.; Johansson, B. *J. Appl. Phys.* **2002**, *92*, 7219−7224.
(36) Correa Baena, J. P.; Steier, L.; Tress, W.; Saliba, M.; Neutzner, S.; Matsui, T.; Giordano, F.; Jacobsson, T. J.; Srimath Kandada, A. R.; Zakeeruddin, S. M.; Petrozza, A.; Abate, A.; Nazeeruddin, M. K.; Grätzel, M.; Hagfeldt, A. *Energy Environ. Sci.* **2015**, *8*, 2928−2934.
(37) Zhou, H.; Chen, Q.; Li, G.; Luo, S.; Song, T.-b.; Duan, H.-S.; Hong, Z.; You, J.; Liu, Y.; Yang, Y. *Science* **2014**, *345*, 542−546.
(38) Xing, G.; Mathews, N.; Sun, S.; Lim, S. S.; Lam, Y. M.; Grätzel, M.; Mhaisalkar, S.; Sum, T. C. *Science* **2013**, *342*, 344−347.
(39) Supasai, T.; Rujisamphan, N.; Ullrich, K.; Chemseddine, A.; Dittrich, T. *Appl. Phys. Lett.* **2013**, *103*, 183906.
(40) Wu, X.; Trinh, M. T.; Niesner, D.; Zhu, H.; Norman, Z.; Owen, J. S.; Yaffe, O.; Kudisch, B. J.; Zhu, X. Y. *J. Am. Chem. Soc.* **2015**, *137*, 2089−2096.
(41) Burschka, J.; Pellet, N.; Moon, S.-J.; Humphry-Baker, R.; Gao, P.; Nazeeruddin, M. K.; Gratzel, M. *Nature* **2013**, *499*, 316−319.

DOI: 10.1021/acs.nanolett.6b04803
Nano Lett. 2017, 17, 1154−1160